MEDICAL DEVICES

A microfluidic wearable device for wound exudate management and analysis in human chronic wounds

Canran Wang[1]†, Kexin Fan[1]†, Ehsan Shirzaei Sani[1,2], José A. Lasalde-Ramírez[1], Wenzheng Heng[1], Jihong Min[1], Samuel A. Solomon[1], Minqiang Wang[1], Jiahong Li[1], Hong Han[1], Gwangmook Kim[1], Soyoung Shin[1], Alex Seder[1], Chia-Ding Shih[3,4], David G. Armstrong[3], Wei Gao[1]*

Chronic wounds are a major global health challenge associated with substantial economic burden and a negative impact on patient quality of life. Real-time analysis of biomarkers like reactive oxygen and nitrogen species could guide treatment, but existing systems lack the capacity required for continuous monitoring. Wound exudate is secreted slowly and has a complex composition, making efficient fluid collection and real-time analysis challenging. To address these issues, we introduce iCares, a wearable device for wound exudate management and continuous in situ analysis of wound biomarkers. iCares contains a flexible nanoengineered sensor array that measures reactive species such as NO, H_2O_2, and O_2, along with pH and temperature, providing multiparameter data to inform wound status. The device features pump-free triad microfluidic modules with a superhydrophobic-superhydrophilic Janus membrane, bioinspired wedge channels, and three-dimensional graded micropillars for efficient unidirectional exudate collection, transport, and refreshing. The sensors demonstrated a consistent response and analyte selectivity in vitro and in wound exudate. iCares was designed for rapid scalable manufacturing through advanced printing and laser patterning. Wireless connectivity supported long-term continuous monitoring in wounds. The iCares system real-time monitoring was tested in a murine model of diabetic skin wound during infection and antimicrobial treatment. Clinical wound evaluation was conducted in 20 patients with chronic wounds and in two patients before and after surgery. A machine learning analysis of the multiplexed data successfully classified wounds and healing times, indicating that wound exudate analysis by iCares could offer insight into chronic wound status to aid in treatment decisions.

INTRODUCTION

Chronic wounds constitute a substantial global health challenge, inflicting considerable economic burdens and profoundly affecting patient quality of life (*1*–*3*). Accurately predicting wound healing status is essential for informed decision-making and timely personalized interventions tailored to patient-specific needs, potentially reducing recovery time and improving overall outcomes. Classification systems such as the Wagner scale evaluate specific factors, such as infection and ischemia, using binary outcomes and without quantitative descriptions (*4*). These classifications are only moderately reliable when scored by multiple experienced clinicians (*5*, *6*), failing to capture the dynamic nature of healing processes. However, frequent wound evaluations for early infection detection and treatment outcome prediction depend on the access to clinical visits for professional examination by wound care experts. These challenges are particularly acute in resource-limited settings and in developing countries. There is a clear demand for more detailed, day-to-day assessments of wound conditions, allowing for a dynamic and responsive approach to wound management, optimizing therapy based on the current state of the wound rather than a static categorization.

Wound exudate is produced during the normal process of wound healing to maintain moisture balance and facilitate nutrient delivery and immunomodulation. In nonhealing wounds, exudate production may persist excessively because of ongoing inflammation or other underlying factors, thereby serving as a potentially valuable source of biomarkers of the wound status. Despite extensive research, there is a lack of technologies for efficient wound exudate sampling and analysis from animals or human patients (*7*–*9*). Recent advances in wearable electronics have shown promise for enhanced wound care (*10*–*17*). Despite these advancements, managing and analyzing wound exudate efficiently remains challenging. Unlike gland-produced biofluids, wound exudate oozes at a rate of 1 to 10 μl cm^{-2} $hour^{-1}$, complicating its collection and analysis (*18*, *19*). In addition, distinguishing between fresh or old exudate is difficult because of limited volume. Approaches like enhanced absorption dressings, microneedles, and microfluidic-based sampling offer potential solutions, but none has achieved efficient collection of inherently limited wound exudate, which contains dense solids such as proteins, dead cells, and debris (*8*, *20*, *21*). Furthermore, the complex matrix of wound exudate poses major challenges for developing biosensors that can perform accurate in situ analysis.

Real-time knowledge of the wound's condition allows for rapid adaptation of treatment plans. Among the key indicators of wound health are the concentrations of reactive species, such as nitric oxide (NO), hydrogen peroxide (H_2O_2), and oxygen (O_2), which serve as biomarkers for tissue perfusion, inflammation, and infection (*7*, *22*–*28*). However, the transient and reactive nature of these species, coupled with the minimal volume of wound exudate, complicate their quantification. This highlights a critical gap in current wound management practices and underscores the need for approaches that accurately reflect healing trajectory and inform personalized interventions.

[1]Andrew and Peggy Cherng Department of Medical Engineering, Division of Engineering and Applied Science, California Institute of Technology, Pasadena, CA 91125, USA. [2]Department of Materials Science and Engineering, University of Central Florida, Orlando, FL 32816, USA. [3]Southwestern Academic Limb Salvage Alliance (SALSA), Department of Surgery, Keck School of Medicine of the University of Southern California, Los Angeles, CA 90033, USA. [4]Casa Colina Hospital and Centers for Healthcare, Pomona, CA 91767, USA.
*Corresponding author. Email: weigao@caltech.edu
†These authors contributed equally to this work.

To address these challenges, we propose a wearable smart bandage designed for wound exudate sampling and in situ continuous analysis of reactive species (iCares). iCares integrates a multiplexed sensor array with a microfluidics architecture for continuous exudate collection, sampling, and refreshing. We tested iCares for wound exudate sampling and in vivo analysis in both mice and human patients with chronic wounds. During long-term mouse monitoring, early changes in sensor readings consistent with early infection were detected from the sensor data before visible symptoms appeared. In a cohort of 20 human patients with venous or diabetic wounds, artificial intelligence (AI)–augmented sensor data enabled accurate wound and outcome classification.

RESULTS

Design of iCares, a wearable device for wound exudate sampling

The iCares system is worn over a chronic wound and was designed to enable continuous efficient collection, transport, and refreshing of small-volume wound exudate for biomarker analysis (Fig. 1A, fig. S1, and table S1). The device features a pump-free triad of microfluidic modules incorporating a superhydrophobic-superhydrophilic Janus membrane to encourage wound fluid entrance to the device, a bioinspired wedge channel to draw wound fluid into the sensor, and a three-dimensional (3D) graded micropillar design to traffic fluid out of the sensor module for dynamic evaluation (Fig. 1B). The integrated flexible nanoengineered sensor array was designed to measure reactive species, including NO, H_2O_2, and O_2, along with pH and temperature, in situ in the complex wound environment for the assessment of wound status (Fig. 1C). The iCares patch can be rapidly manufactured at scale and at low cost using drop-on-demand inkjet printing, laser engraving, and 3D printing (Fig. 1, D and E, and figs. S2 to S4). To enable wireless, continuous, and long-term monitoring of reactive species on wounds, the fully integrated iCares system was vertically stack-assembled with a printed circuit board (PCB) for data acquisition, processing, and wireless communication (Fig. 1, F and G, and figs. S5 to S7). The completely assembled device was encapsulated in polydimethylsiloxane (PDMS) and

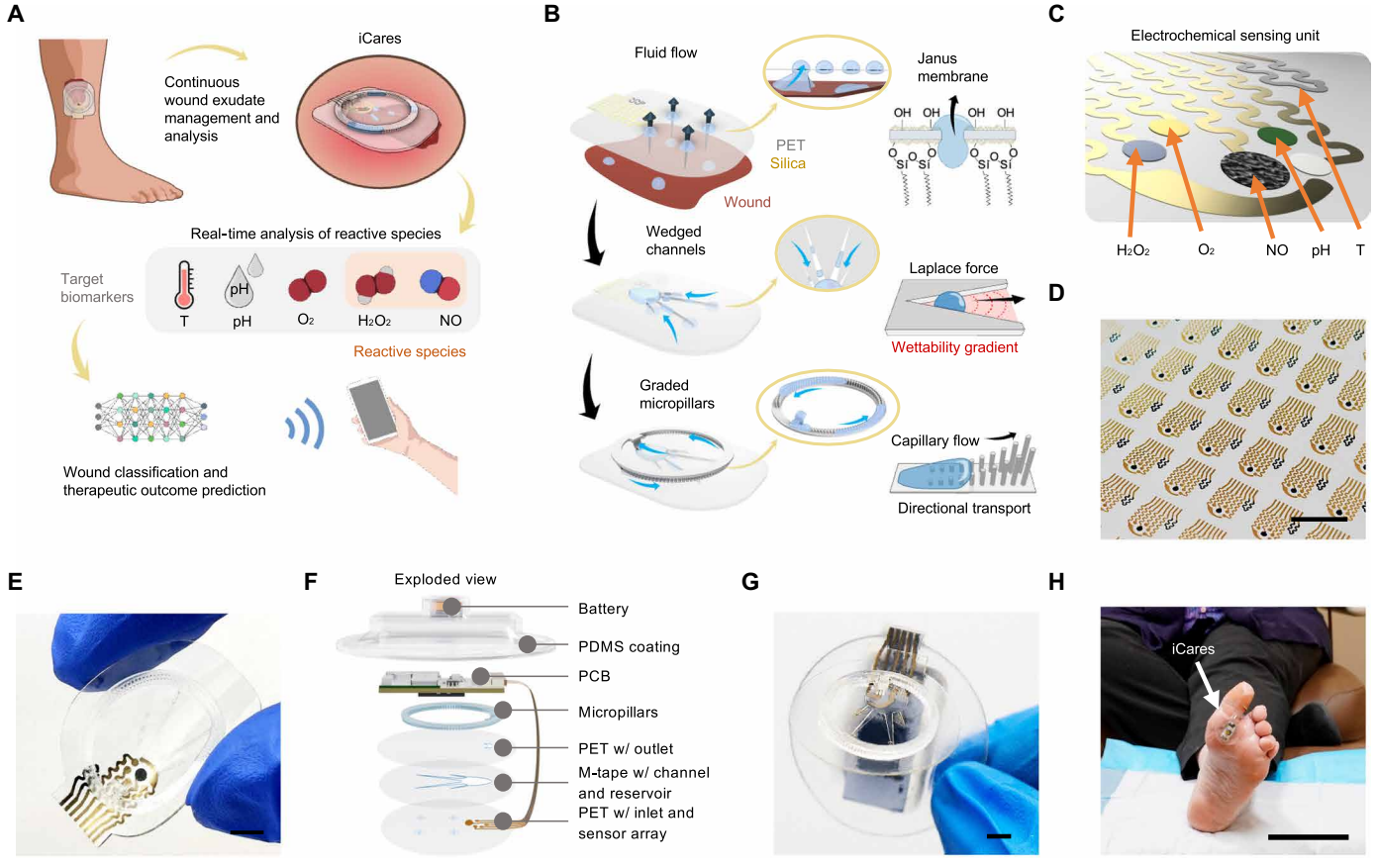

Fig. 1. iCares, a wireless smart bandage for wound exudate management, reactive species analysis, and personalized wound assessment. (**A**) Schematics of the integrated iCares system applied on a chronic wound. iCares was designed with a sensor array and triad microfluidics and integrated with wireless communication modules for real-time data analysis. T, temperature sensor. (**B**) Design of the triad microfluidic modules incorporating the Janus membrane, wedged channels, and graded micropillars for efficient collection, transfer, and refreshing of wound exudate. (**C**) Schematic of the electrochemical sensing array for multiplexed reactive species analysis. The diameter of pH, O_2, and H_2O_2 sensors, 1 mm; the diameter of NO sensor, 2 mm; the width of printed gold and carbon lines, 600 μm. (**D**) Photograph of sensor arrays mass produced by inkjet printing. Scale bar, 1 cm. (**E**) Photograph of an assembled iCares patch. Scale bar, 5 mm. (**F**) Exploded view of the assembled iCares patch. The layers, from bottom to top, include a PET layer with an inlet and sensor array, medical tape (M-tape) with microfluidic channels and reservoir, PET with an outlet, micropillars, a PCB for data processing and wireless communication, a protective PDMS coating, and a battery for power. (**G**) Photograph of the fully integrated wireless iCares system. Scale bar, 5 mm. (**H**) Photograph of an iCares device worn by a patient with a diabetic ulcer in the clinical setting. Scale bar, 10 cm.

is compatible with medical wound dressings, such as Tegaderm, for placement on human chronic wounds (Fig. 1H) or murine preclinical wounds (fig. S7).

Pump-free microfluidics for efficient wound exudate management

Efficient wound exudate management including sampling, transport, and refreshing was achieved through a design consisting of a triad of microfluidic modules with design strategies of geometric structure and wettability gradients including a Janus membrane, a wedge channel, and a micropillar array (Fig. 2A). To address the challenge of collecting low-volume exudate directly from the wound surface, we used a Janus membrane in the collection layer with highly asymmetric surface hydrophobicity whereby the side facing wound was superhydrophobic, whereas the opposite side was superhydrophilic. Durable wettability gradients, incorporating both superhydrophilic and superhydrophobic surfaces, were created by directly spraying 1*H*,1*H*,2*H*,2*H*-perfluorooctyltriethoxysilane–coated dendritic silica onto a polyethylene terephthalate (PET) surface with or without additional O_2 plasma treatment, respectively (Fig. 2B). Consistent contact angles of 165° (hydrophobic surface) and 0° (hydrophilic surface) with simulated wound fluid (SWF) were maintained for over 4 days for the superhydrophilic and superhydrophobic surfaces, respectively (Fig. 2B and fig. S8). The silica coating maintained over 90% transparency,

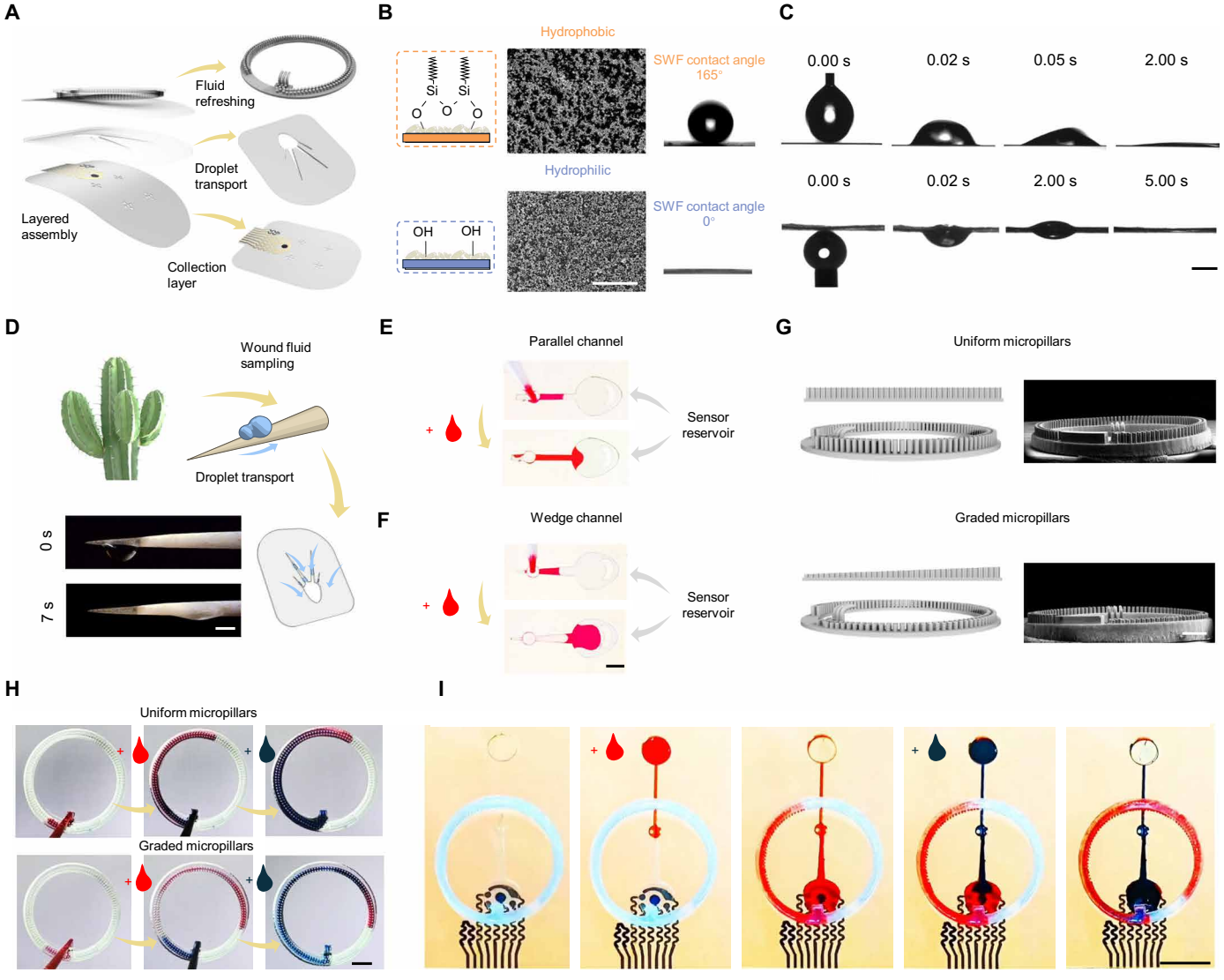

Fig. 2. Design and characterization of the triad microfluidic modules for efficient wound exudate management. (**A**) Schematic of the triad microfluidic modules for wound exudate collection, transfer, and refreshing. (**B**) Schematics, SEM images, and contact angle test images showing the superhydrophobic (top) and superhydrophilic (bottom) surfaces based on silica-coated PET films. Scale bar, 10 μm. (**C**) Photographs of the Janus membrane inlet for exudate collection and unidirectional transport from wound bed to the upper side. Scale bar, 2 mm. (**D**) Illustrations of cactus-inspired fluid automated transfer. Photograph of transport of a 2-μl water droplet along the cactus spine. Scale bar, 2 mm. (**E** and **F**) Representative photographs of 2 μl of red dyed SWF transportation in parallel (E) and wedged-shape (F) channels toward the sensor reservoir. Scale bar, 1 mm. (**G**) Schematic (left) and SEM images (right) of micropillar arrays with uniform and graded micropillar heights. Scale bar, 1 mm. (**H**) Photographs of SWF transport (2 μl of red and blue SWF, sequentially) on uniform and graded micropillar arrays. Scale bar, 2 mm. (**I**) Representative time-lapse photographs showing automatic transport of SWF in the assembled triad microfluidic modules (10 μl of red SWF followed by 5 μl of blue SWF). Scale bar, 5 mm.

allowing for visual assessment of wound conditions in clinical settings when used as a dressing material (fig. S9). There are four inlets with a diameter of 1 mm in the collection layer. Rapid and unidirectional liquid transport of the curved water droplets through the laser-patterned micropores of the Janus membrane (100 μm in diameter, spaced 100 μm apart) was achieved owing to the Laplace pressure resulting from the high wettability gradient (Fig. 2C, fig. S10, and movie S1). Compared to narrower micropore channels, our design showed faster transportation in simulation (fig. S11).

Transport of the slowly generated low-volume wound exudate to the sensor patch for timely analysis is necessary for assessment of labile reactive species. Here, we designed a wedge-shaped channel for wound fluid collection inspired by the moisture-collecting capabilities of cactus spines (Fig. 2D and movie S2). Compared with a parallel transport channel, a wedge-shaped transport channel directed 2 μl of SWF to a sensing reservoir more efficiently (Fig. 2, E and F, and movie S3). We simulated channels with different angles and found that our design (6°) enabled faster automated fluid transfer compared with wider (20°) or narrower (3.5°) designs (fig. S12).

Considering that wound exudate oozes out very slowly, the new exudate often mixes with the old one, making real-time analysis highly challenging. To address this challenge, the iCares system was designed with a 3D graded height micropillar array to create directional capillary forces, resulting in unidirectional and automatic transfer of old fluid out of the sensing reservoir (Fig. 2, G and H, and fig. S13). Finite element simulations demonstrated that the graded micropillars facilitate faster automated fluid transfer (fig. S14). To test fluid mixing, we added red and blue dyed fluids in series to the uniform or graded micropillar designs. Unlike a uniform pillar design, the graded structure effectively minimized the mixing of two fluid samples (Fig. 2H and movie S4), substantially enhancing the temporal sensing resolution. Each microfluidic module was optimized and validated using numerical simulations based on finite element analysis (FEA) (movie S5).

Together, the triad of microfluidic modules collected, transported, and refreshed small volumes of fluid without a pump. After we gently dropped 5 μl of colored SWF onto the hydrophobic side of the Janus membrane, the system automatically and efficiently collected all of the fluid into the channel and sensing reservoir. We scanned the NO sensor every 1 min and measured the H_2O_2 sensor continuously. Minimal mixing of the differently dyed SWF drops was observed at the sensor reservoir. The first SWF with the red dye was directed out of the sensor reservoir and into the graded micropillar structure, followed by blue dyed SWF filling the reservoir (Fig. 2I and movie S6), supporting the ability of the device in managing and controlling wound fluid.

To evaluate the biocompatibility and cytocompatibility of the iCares sensor patch, we analyzed the cell viability and metabolic activity of human dermal fibroblasts (HDFs) cultured in direct contact with the microfluidic sensor patch using a commercial cell live/dead kit and the PrestoBlue assay. The results showed that HDFs maintained normal cellular morphology and exhibited cell viability and metabolic activities comparable to those of the control group over the multiday culture period (fig. S15). This indicates the good cytocompatibility of the iCares patch, making it suitable for subsequent in vivo studies in both animal and human trials.

Design and characterization of the multiplexed sensor patch for reactive species analysis

For biomarker analysis in wound exudate, we developed a flexible, multiplexed, nanoengineered electrochemical biosensor array. This array consists of a voltammetric NO sensor, a voltammetric O_2 sensor, an amperometric H_2O_2 sensor, a potentiometric pH sensor, and a resistive temperature sensor (Fig. 3A). To facilitate electrochemical sensing, a shared polyvinyl butyral (PVB)–coated Ag/AgCl reference electrode and a gold nanoparticle (AuNP)–based counter electrode were incorporated.

Sensitive and selective NO sensing was achieved using a laser-engraved graphene (LEG)/graphene oxide (GO) electrode immobilized with hemoglobin (Hb) as the recognition receptor (Fig. 3, B and C). Hb cannot be absorbed into LEG directly; therefore, we coated LEG with GO dispersed in a surfactant [hexadecyltrimethylammonium bromide (CTAB)], allowing electron transfer from the porphyrin center of Hb to the electrode and expanding the electrode's surface area. Most existing NO sensors operate at a positive potential to quantify the oxidation of NO, which substantially compromises selectivity because of the presence of various electroactive interferences, such as H_2O_2, uric acid, and amino acids, in the wound exudate (*29*–*31*). Hb contains a porphyrin complex of iron(II), known as NO reductase, which converts NO into nitrous oxide (N_2O). To ensure accurate NO sensing, we used an Hb-based strategy that detects NO reduction at a potential of ~−0.8 V using differential pulse voltammetry (DPV) (Fig. 3B) (*31*). The LEG/GO electrode offers high electrocatalytic performance owing to the mesoporous graphene structure and rapid electron transfer, resulting in superior sensitivity for NO analysis compared with other electrode materials (figs. S16 and S17). The optimized LEG/GO-based sensors demonstrated a linear relationship between the reduction peak height current and physiologically relevant NO concentrations in SWF, with high selectivity over the potential interfering molecules and a low detection limit of 0.5 μM (Fig. 3B and fig. S18). The sensitivity of the NO sensor was optimized by adjusting laser engraving parameters (fig. S19). In this case, we demonstrated an NO sensor that is both mechanically flexible and highly selective over electroactive molecules, making it ideal for wound monitoring applications (table S2). Similarly, highly sensitive O_2 sensing with a wide detection range [1.26 to 6.57 parts per million (ppm)] was realized through the quantification of O_2 reduction at around −0.15 V on an inkjet-printed AuNP electrode, with the measured DPV reduction peak height current showing a linear correlation with O_2 concentrations (Fig. 3, D and E).

We designed the H_2O_2 sensors based on electrodeposited Prussian blue (PB), which serves as an efficient catalyst for H_2O_2 reduction (Fig. 3, F and G). The amperometric sensor response exhibited a linear correlation with the H_2O_2 concentrations, with a sensitivity of 5.91 nA μM^{-1} and detection limit of 0.25 μM (Fig. 3H). Our optimizations indicated that a Nafion permselective coating substantially enhances the sensing performance in biologically relevant fluids owing to its antifouling properties (fig. S20). In addition, to enhance the stability of PB in a neutral or alkaline wound environment, we incorporated a PB analog nickel hexacyanoferrate (NiHCF) on top of the PB film (*32*). This layering technique forms a robust composite structure that yielded a highly stable sensor response with minimal signal drift, maintaining consistent performance both SWF and wound exudate collected from diabetic mice (figs. S21 and S22).

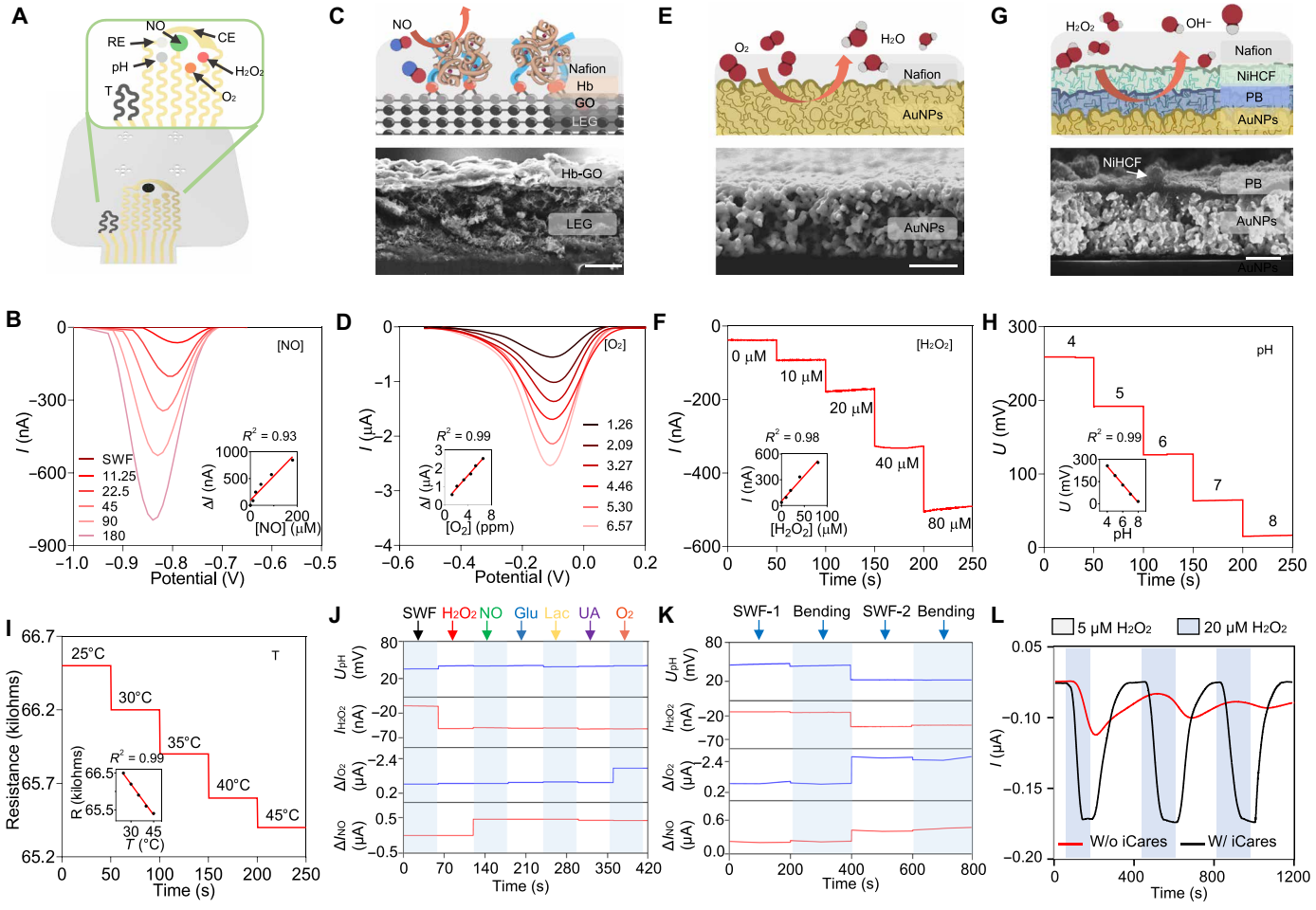

Fig. 3. Design and characterization of a multiplexed sensor array for reactive species analysis. (**A**) Schematic of a sensor array. (**B**) Representative DPV responses of the NO sensor in SWF. Inset: calibration plot with a linear fit. *I*, current; Δ*I*, peak current density height. (**C**) Schematic of the mechanism and SEM images of an LEG/GO electrode for NO sensing. Hb, hemoglobin. The thickness of the Hb-GO layer is 8 μm, and that of the LEG layer is 25 μm. Scale bar, 15 μm. (**D**) DPV voltammograms of the O_2 sensor in SWF. Inset: calibration plot with a linear fit. (**E**) Schematic and SEM images of an inkjet-printed AuNP electrode for O_2 detection. The thickness of the AuNP layer is ~600 nm. Scale bar, 500 nm. (**F**) Amperometric responses of the H_2O_2 sensor in SWF. Inset: calibration plot with a linear fit. (**G**) Schematic and SEM image of a Ni-HCF/PB-coated AuNP electrode for H_2O_2 detection. The thickness of the PB layer is 30 nm, and that of the AuNP layer is 600 nm. Scale bar, 400 nm. (**H**) Potentiometric response of a polyaniline-based pH sensor. Inset: calibration plot with a linear fit. (**I**) Resistive response of an inkjet-printed carbon temperature sensor. Inset: calibration plot with a linear fit. (**J**) Multiplexed sensing responses of a sensor array upon adding common interference and target molecules: 10 μM H_2O_2, 20 μM NO, 30 mM glucose (Glu), 200 μM lactic acid (Lac), 100 μM uric acid (UA), and 5 min O_2 bubbling. (**K**) Responses of a sensor array before and after mechanical bending in SWF on a glass cyclic tube at the 50th cycle in 10 min (SWF-1: pH 7 with N_2 bubbling for 5 min and 10 μM NO; SWF-2: pH 7.5 with 10 μM H_2O_2, N_2 bubbling for 1 min and 20 μM NO). Radius of bending curvature, 2.5 cm. (**L**) Amperometric responses of a H_2O_2 sensor within and without the triad microfluidic modules upon switching SWF solutions containing 5 and 20 μM H_2O_2. For (B), (D), (F), and (H) to (L), $n = 1$ technical replicate per group.

All three reactive species sensors demonstrated high stability after multiday incubation in SWF (figs. S20, S23, and S24) and after 30-day storage (fig. S25), indicating their potential for in situ continuous wound exudate analysis. The pH of the solution could influence the responses of NO, O_2, and H_2O_2 sensors (figs. S26 to S28); therefore, we developed and incorporated a pH sensor based on an electropolymerized polyaniline film (Fig. 3H). The pH sensor maintained a stable potentiometric response when exposed to SWF for at least 3 days (fig. S29). Temperature could also influence the sensor readings, so we evaluated the pH, NO, O_2, and H_2O_2 sensors at differing temperatures between 25° and 45°C to establish calibration curves for each parameter (figs. S30 to S33). A temperature sensor based on printed carbon was incorporated into the sensor patch for real-time calibration (Fig. 3I). Linear responses were observed between the resistive response and physiologically relevant temperature concentrations for the temperature sensor and between the measured potential changes and pH concentrations (Fig. 3, H and I). We also further validated the performance of NO and H_2O_2 sensors in human serum spiked with known concentrations of the analytes. Both sensors exhibited comparable sensitivity (9.75 nA μM^{-1} in SWF and 9.22 nA μM^{-1} in serum) within a detection range from 0 to 45 μM NO, maintaining a linear response in SWF (figs. S34 and S35).

The iCares sensor patch was capable of simultaneous, selective, and multiplexed monitoring of target analytes in SWF without interference between targeted biomarkers (Fig. 3J). Owing to its high

mechanical flexibility, the sensor patch maintained stable multiplexed sensor responses under repetitive mechanical deformations, underscoring its practical usability during daily physical activities (Fig. 3K).

To validate the real-time sensing performance of the microfluidic system for reactive species analysis, dynamic biosensing was conducted using the fully assembled microfluidic sensor patch with consecutive drops of SWF containing varying H_2O_2 or NO concentrations (Fig. 3L and fig. S36). When the H_2O_2 concentrations in the newly added SWF were switched between 5 and 20 μM, the system stabilized within ~1 min, providing accurate and stable readings (Fig. 3L). In contrast, tests conducted without the triad microfluidic modules exhibited unstable and inaccurate readings in response to dynamic analyte concentrations. These results further confirmed that the microfluidic design is crucial for efficient wound exudate management and high-performance real-time wound biomarker analysis.

Long-term continuous monitoring of reactive species in vivo

To establish the in vivo function of the iCares device, we examined the performance of the encapsulated wireless platform over 12 hours in an excisional wound model in diabetic mice (Fig. 4A). The conformal contact between iCares and mouse skin allowed them to move freely (Fig. 4B and movie S7). The device remained in place over the dorsal skin wound for the 12 hours of evaluation. To visualize wound fluid collection and transport, a red dye was placed inside the sensor reservoir at the beginning of the study. After 0.5 hour, the red dye was visible within the micropillars' structure, and continued movement of the dye through the gradient micropillars was observed over time with no dye remaining in the reservoir after 6 hours (Fig. 4C). These data indicate that the fluid in the sensor reservoir was refreshed over time. Our test indicated that efficient wound exudate sampling can be realized at a low rate of ~2 μl cm^{-2} $hour^{-1}$ in mouse wounds. In addition, during the 12-hour test, wound exudate rate was lower between 6 and 12 hours after applying iCares compared with the initial hours. This reduction may be attributed to evaporation, effectively delaying system overflow. For individuals with high wound fluid production, the micropillar ring can be removed and replaced to accommodate the increased fluid volume.

Considering that dietary intake influences diabetic individuals and their wound healing environments, we further investigated how the wound exudate composition responds to fasting and feeding in diabetic mice (Fig. 4D). We assessed wound conditions before fasting, after 24 hours of fasting, and again after 24 hours of refeeding. Fasting-induced hypothermia was observed, marked by slightly decreased temperature, which reverted upon refeeding. In addition, H_2O_2 concentrations decreased after the fasting.

An in vivo multiplexed infection monitoring study was then performed by applying the iCares platform to mouse wounds continuously for 3 days (Fig. 4E). The presence of bacteria in the wound and the successful treatment were validated by analysis of proliferative and viable bacteria from wound exudate (figs. S37 and S38). The wound fluid composition was assessed by iCares before infection (day 1), after infection (day 2), and after antimicrobial peptide TCP-25 treatment (day 3), with measurements taken for 2 hours each time. Treatment was applied 24 hours after inoculation, and wound conditions were measured 24 hours posttreatment. In three mice, we observed a general increase in temperature, pH, and H_2O_2 on day 2 (24 hours after infection) and a slight decrease in these measurements after the treatment. No clear trend was observed in O_2 and NO measurements during the study. The group that received antimicrobial treatment showed elevated expression of vascular endothelial growth factor (VEGF) 10 days after initial infection, indicating a potentially improved wound regeneration process with infection treatment (fig. S39).

To evaluate the early warning capability of the iCares platform for infection, we continuously monitored two mice for 54 hours after bacteria inoculation, with treatment administered midway through the monitoring period (Fig. 4, F and G). Despite no visible infection at the wound site in 24 hours after inoculation, substantial sensor signal changes indicated early infection stages. Elevations in temperature, pH, and H_2O_2 were observed within the first 24 hours after inoculation. Immediate treatment led to rapid wound healing and prevented further infection progression, unlike cases with delayed treatment where serious infections developed. We also observed temperature, pH, and H_2O_2 concentration trending back toward normal, indicating the effectiveness of treatment. This emphasizes the importance of timely intervention based on sensor data, underscoring the potential of the iCares platform for early detection and enhanced wound management outcomes.

We assessed the biocompatibility of the iCares patch by subcutaneously implanting it in mice for up to 28 days compared to a sham surgery on the skin. Initial assessments involved hematoxylin and eosin (H&E) staining to evaluate tissue morphology and response (Fig. 4, H and I). The cross section of skin implanted with iCares indicated normal interfacing between the device and subcutaneous tissue. Qualitative assessment of nascent epidermal thickness and immune cells in the dermis, identified by cell morphology and polymorphonuclear presence, showed no difference between sham and implant groups. Subsequent immunofluorescence staining revealed the minimal presence of leukocyte (CD3) and macrophage (CD68) after 14 and 28 days of implantation (Fig. 4, J and K). These results showing normal tissue morphology with negligible inflammatory cell infiltration or adverse reactions support the compatibility of the iCares platform with biological tissues.

Evaluation of iCares on patients with chronic wounds for AI-powered wound management

The efficient fluid collection and multiplexed sensing capabilities of iCares were next tested for continuous real-time monitoring of chronic wounds in patients. We developed machine learning algorithms for the evaluation of multiplexed sensor data toward the goal of personalized chronic wound management (fig. S40). We evaluated the use of iCares in 20 patients with chronic nonhealing lower extremity ulcers due to venous insufficiency and diabetes. Future studies will include an expanded range of wound types, such as pressure ulcers and burns. Patient health information, including age, wound area, and peripheral artery disease (PAD), as well as the healing time since the test, was collected for data analysis (Fig. 5A and table S3). Integrating iCares with a standard Tegaderm wound dressing ensured conformal and consistent application on both types of chronic wounds (Fig. 5, B and C). All sensor signals were calibrated and normalized to ensure that the features extracted after data preprocessing were stable and accurate, accounting for patch variations and moderate motion artifacts (Fig. 5, D to F). As a result, the calibrated oxygen sensing results showed a high Pearson correlation coefficient of 0.943 with the US Food and Drug Administration–approved oxygen measuring device by Kent Imaging (figs. S41 and

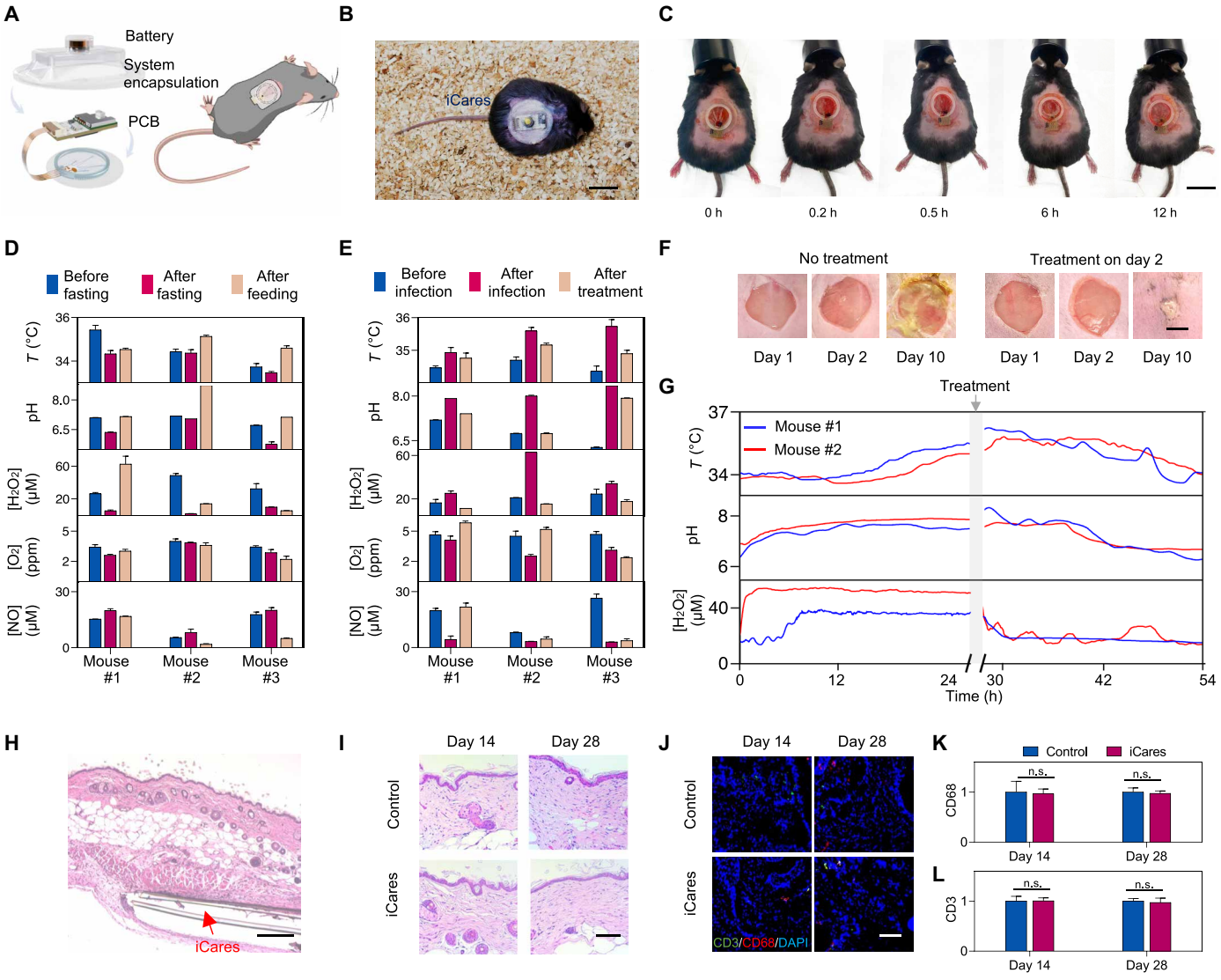

Fig. 4. In vivo evaluation of iCares using a diabetic mice model. (**A**) Schematic of the fully assembled and encapsulated iCares system applied to a mouse with a chronic wound on its back. (**B**) Photograph of a freely moving diabetic mouse wearing iCares in a cage. Scale bar, 2 cm. (**C**) Representative images of in vivo wound exudate continuous sampling using iCares on a mouse after indicated time points. The mouse was awake and freely moving between image taken at 0.5, 6, and 12 hours (h). Concentrated red dye was added to the reservoir before application to the mouse for visualization. Scale bar, 2 cm. (**D**) In vivo multiplexed sensing response of the iCares devices on diabetic mice with chronic wounds before fasting, after fasting, and after feeding. Data are presented as means ± SD of three measurements in 2 hours within each mouse, with a 1-hour interval between each measurement. $n = 3$. (**E**) In vivo multiplexed sensing response of iCares devices on diabetic mice before infection, after infection, and after treatment of the chronic wounds. Data are presented as means ± SD of three measurements in 2 hours, with a 1-hour interval between each measurement. $n = 3$. (**F**) Representative photographs of infected wounds on mice with or without timely antimicrobial peptide treatment on day 2 (infection on day 1). Scale bar, 5 mm. $n = 3$. (**G**) Representative continuous multiplexed wound biomarker monitoring in vivo over 54 hours in mice using iCares in response to infection and treatment. $n = 2$. (**H** and **I**) H&E staining of iCares-implanted mouse tissue (H) and conditions of the tissue adjacent to the implantation and control tissue (I) on day 14 and day 28. Scale bars, 200 μm. $n = 3$. (**J** to **L**) Fluorescence images (J) and quantitative analysis of CD68 (K) and CD3 (L) expression in iCares-implanted mouse tissue and control tissue. Scale bar, 100 μm. Analysis by unpaired two-way Student's *t* test. Data are presented as means ± SD. n.s., not significant. $n = 3$.

S42), validating the accurate performance of our wearable sensors across various wound types and sizes.

For two patients undergoing vascular intervention surgeries, we evaluated two sessions of on-body data capture, one 7 days before surgery and either 14 or 20 days after surgery. These studies revealed changes in wound sensor readings after the procedures (Fig. 5, D and E). In both patients, we observed an increase in O_2 and NO and a decrease in pH after surgery, whereas H_2O_2 showed divergent trends between the two individuals. Clinical wound assessment tools, such as wound classification, predicted healing time, and wound depth, play important roles in patient wound care but are often reliant on personal experiences and require multiple clinicians to evaluate them consistently (*5*, *6*, *33*). To overcome these challenges, we applied machine learning models to extract features from the multimodal data collected iCares. These models deconvolute connections between physicochemical signals, patient

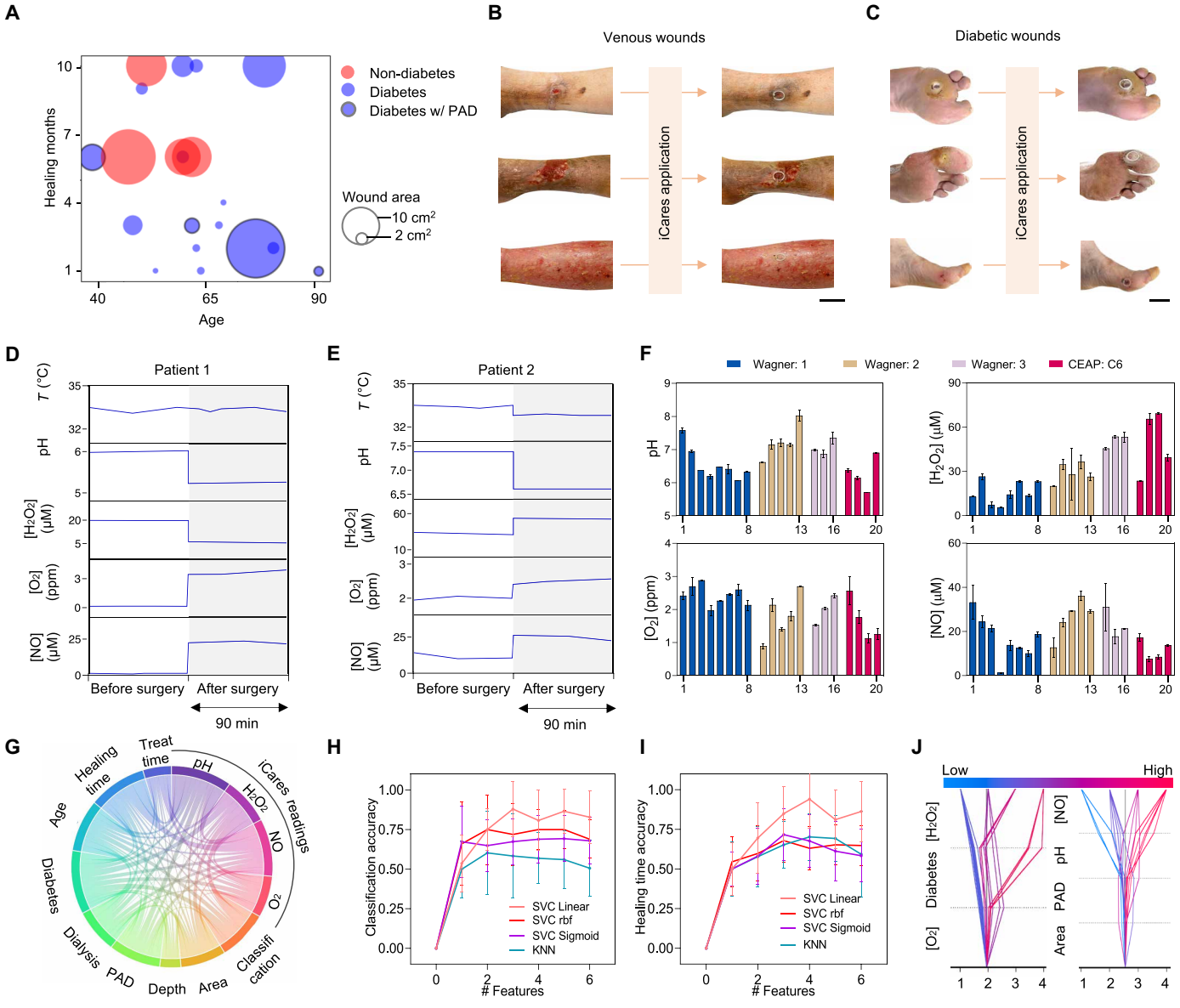

Fig. 5. AI-powered in vivo evaluation of iCares in patients with chronic wounds. (**A**) Bubble plot of participant and wound information. Bubble area, wound size; red, venous wound, blue, diabetic wound; solid black border, PAD. (**B** and **C**) Representative images of venous wounds (B) and diabetic wounds (C) before and after iCares applications. Scale bars, 3 cm. (**D**) Multiplexed monitoring of wound biomarkers in patient 1, 7 days before and 14 days after vascular intervention surgery. (**E**) Multiplexed monitoring of wound biomarkers in patient 2, 7 days before and 20 days after vascular intervention surgery. (**F**) Multiplexed molecular sensing results from 20 patients with labeled chronic classifications. Data are presented as means ± SD from three time points (0, 1, and 2 hours) after monitoring initiation; each bar represents one participant. $n = 20$. CEAP, clinical, etiological, anatomical, and pathophysiological. (**G**) Chord diagram showing the Pearson correlation between biomarker concentrations, patient health conditions, and wound status. (**H** and **I**) Wound classification (H) and healing time (I) accuracy based on different machine learning models and features used. Features in (H) progress from H_2O_2 only to combinations with pH, diabetes, dialysis, PAD, and age. Features in (I) progress from NO only to combination with pH, wound area, PAD, age, and dialysis. Error bars represent the SD of the mean from three ML results. SVC, support vector classification; Rbf, radial basis; KNN, *k*-nearest neighbor algorithm. (**J**) SHAP decision plot explaining how the ML model determines wound classification (left) and healing time (right) using combinations of biochemical and patient features. Color scale, low (blue) to high (magenta). For wound classification (left), the outputs 1, 2, 3, and 4 represent Wagner grade 1, Wagner grade 2, Wagner grade 3, and CEAP C6, respectively. For wound healing time prediction (right), 1, 2, 3, and 4 represent less than 1 month, from 2 to 5 months, from 6 to 9 months, and over 10 months, respectively.

information, and wound conditions (Fig. 5G). The chord diagram visually represents the intricate relationships between various patient characteristics and biochemical markers related to wound healing. Factors such as age, diabetic status, and PAD intricately interact with parameters like pH, H_2O_2, NO, and O_2 concentrations, contributing to wound status. The relatively homogeneous correlation demonstrates the high independence of the sensor readings from iCares.

Using the features extracted from the patient data and iCares measurements, we classified the wounds and healing time using several different models. Through Shapley additive explanation (SHAP) analysis of the feature relevance (*34*), we determined that diabetes,

O_2, and H_2O_2 played the most important roles in classifying wounds, whereas PAD, wound area, pH, and NO were important for predicting healing time, achieving classification accuracies of 88.75 and 94.0%, respectively, using a support vector classification (SVC) linear model (Fig. 5, H to J, and fig. S43). We also used features such as NO, H_2O_2, diabetes, and age to estimate wound depth with an accuracy of 81.4% (fig. S44). These models are based on our single cohort of 20 individuals and will need to be further validated with an independent cohort to establish generalizable predictability.

DISCUSSION

Compared with the previously reported wound care wearables, iCares offers a substantial advance by allowing in vivo wound exudate sampling directly from the wound site, enabling instantaneous and refreshable in situ biochemical analysis (table S4). Given the highly variable composition and low volume of wound exudate, iCares uses a triad microfluidic architecture with meticulously designed geometric structures and wettability gradients, ensuring consistent sample acquisition and refreshing. Moreover, iCares uses nanoengineered materials and highly specific bioreceptors with protective layers, effectively overcoming interference from electroactive molecules, proteins, cellular debris, and external contaminants. This design enables wearable wound exudate biomarker analysis.

In the complex cascade of wound healing, reactive species, including H_2O_2, NO, and O_2, play critical multifaceted roles in inflammation, infection control, angiogenesis, and local wound circulation. During the initial inflammatory phase, reactive oxygen species (ROS) signal to recruit monocytes and macrophages to the wound site, facilitating the removal of debris and pathogens (*35*). However, prolonged or excessive H_2O_2 concentration can exacerbate inflammation and delay healing. NO and H_2O_2 and peak during the initial stages postinjury, coinciding with the influx of inflammatory cells, particularly monocytes and macrophages, into the wound site. In our murine studies, iCares measured increases in wound temperature, pH, and H_2O_2 after wound bacterial infection, which is correlated with a previous report (*12*). This suggested iCares' ability to detect early pathological changes, such as infection before visible symptoms, enabling timely intervention and prevention of complications.

In addition to early-stage inflammation, reactive species play a dual role in having antimicrobial properties and regulating the immune response (*36*, *37*). NO induces the production of growth factors like VEGF, enhancing blood flow to the wound site, increasing leukocyte migration, and improving pathogen clearance. In our patient studies, the observed elevation in NO concentration after surgery could be associated with surgically restored blood flow and a likely increase in activity of endothelial nitric oxide synthase (eNOS). This phenomenon underscores surgical interventions in improving vascular function, thereby boosting tissue oxygenation and facilitating healing.

H_2O_2 acts as a potent antimicrobial agent, directly killing bacteria through oxidative stress and recruiting immune cells for enhanced defense (*38*). In the postsurgical wound exudate evaluation, we observed different trends in H_2O_2 between the two individuals assessed. These differing trends in H_2O_2 concentrations may stem from different postsurgery recovery processes, and such discrepancies may reflect comorbidities and timing of postoperative measurements, underscoring the need for personalized care and continuous monitoring. Adequate O_2 supports infection control by promoting tissue oxygenation, which is crucial for immune cell function and efficiency (*39*). Infections are associated with decreased SpO_2. ROS are essential for the early killing of ingested pathogens, whereas reactive nitrogen species (RNS) control pathogen replication during the later stages of infection. At low concentrations, H_2O_2 facilitates wound angiogenesis in vivo by inducing focal adhesion kinase (FAK) phosphorylation and VEGF production (*40*). Understanding and managing the concentration and effects of H_2O_2, NO, and O_2 within the wound milieu are critical, whereas imbalance in these species can lead to poor healing outcomes, such as chronic wounds or excessive scarring. The iCares system provides multiplexed and multimodal sensing, combined with modern machine learning algorithms, to provide a real-time assessment of wound healing status without the need for subjective or historical information.

NO plays a pivotal role in multiple metabolic signaling pathways in a concentration-dependent manner. In vivo NO concentration is regulated mainly by the bioavailability of the L-arginine NO synthase pathway and boosted by the nitrate–nitrite–nitric oxide pathway by diet (*41*). Overproduction of NO serves as pro-inflammatory mediation, whereas NO deficiency results in an oxidative stress–derived pathological process (*42*). For example, reduced NO production can cause attenuation of glucose-induced insulin secretion, hepatic glucose output, and browning of white fat process, which is commonly found in the pathological process of type 2 diabetes mellitus, obesity, and increased blood pressure (*43*–*45*). On the other hand, high NO and superoxide concentration form peroxynitrite, leading to endothelial dysfunction and obesity-related hypertension (*41*, *46*) and a series of liver diseases, such as nonalcoholic fatty liver disease and biliary cirrhosis (*47*).

Current understanding of in vivo NO concentration is mainly based on indirect analysis of NOS activity or NOx species concentration (*48*). Wearable biosensors for NO sensing in biofluids are scarce because of various interferences. To enable selective quantification of NO in vivo, we propose a biosensing approach by immobilizing Hb on LEG. Hb contains a porphyrin complex of iron(II), known as NO reductase, which converts NO into nitrous oxide (N_2O). Because Hb cannot bind directly to LEG, we coated the electrode with GO in a surfactant (CTAB) to facilitate electron transfer and increase the surface area. The preparation was optimized for broad linear sensitivity and high selectivity against common biofluid metabolites. Our wearable sensor is capable of NO monitoring in wound fluid, distinguishing it from other electroactive molecules.

Our machine learning model is designed to classify wound healing outcomes using wound exudate chemical signals and objective and quantitative data inputs such as age and the presence of PAD for first-time patients with chronic wound. This approach enables for the potential to classify both venous and diabetic chronic wounds for potential for healing without the need for subjective or historical data such as wound classification scores or patient visit frequency, which are commonly relied upon by other models (*49*–*51*). By focusing on measurable and reproducible data, our approach not only improves accessibility and usability for first-time patients but also enhances the model's generalizability and robustness. In the future, this framework could be adapted to predict a broader range of pathological conditions, offering a versatile tool for diagnosing and managing diverse medical conditions in a timely and efficient manner. In addition, this approach avoids potential biases associated with variations in hospital care quality and clinician estimation,

ensuring more consistent and reliable results, particularly in developing countries and resource-limited settings.

Our study presents promising preliminary data on wound exudate sampling, monitoring, and analysis. However, there are several limitations that should be considered. First, although the iCare system is designed to be flexible, its fixed shape restricts its ability to conform to wounds with varying depths, irregular contours, or dynamic changes during healing. This constraint may reduce its applicability for certain wound types that require adaptive coverage for optimal monitoring and treatment. Second, iCare components can be manufactured at scale using laser cutting, inkjet printing, and 3D printing; the assembly process requires precise alignment and manual operations. This complexity may pose challenges for large-scale production and consistency, potentially affecting reproducibility. Third, the iCare system is designed primarily for monitoring and does not include an integrated treatment module. For instance, O_2 plays a crucial role in wound healing by enhancing local circulation, supporting cellular functions, and maintaining overall tissue health. Insufficient oxygenation can lead to tissue hypoxia, which can severely impair wound healing by restricting cellular respiration and energy production. In the future, integrating therapeutic components, such as controlled O_2 delivery or drug release, could further enhance the system's functionality and improve wound healing outcomes. Another key limitation is the lack of sufficient clinical validation given that the correlations between wound status and various biomarkers in wound exudate remain incompletely established. Addressing this gap requires comprehensive clinical trials to validate our findings and enhance the predictive accuracy of these biomarkers across different wound conditions. By conducting extensive clinical trials across diverse patient populations to validate system effectiveness and reliability, we anticipate that future investigations will substantially enhance chronic wound management, offering a more precise, data-driven approach to improve patient care and treatment outcomes while reducing the burden on healthcare providers.

MATERIALS AND METHODS

Study design

The primary objective of this study was to develop and validate a device for sampling wound exudate volume and analyzing wound status and therapeutic outcome through real-time monitoring of temperature; pH; and concentrations of oxygen, hydrogen peroxide, and nitric oxide in bacterially infected murine diabetic skin wounds and in human chronic wounds from venous insufficiency or diabetes. We optimized and validated the device design and sensor function in vitro with SWF. Biocompatibility was assessed by direct culture with HDFs in vitro and by subcutaneous implantation in mice. Machine learning techniques were used to evaluate the multiplex sensor data, clinical wound data, and patient characteristics. This study was conducted in accordance with the protocol approved by the Institutional Review Board (IRB) at the Casa Colina Hospital and Centers for Healthcare in Pomona, CA (protocol number 00002372). The clinical study was not blinded and involved 20 patients with venous ulcers or diabetic wounds as volunteers. There was no randomization given the observational nature of the study. The inclusion criteria were as follows: age ≥ 18; with or without diabetes mellitus; and with an ulcer diameter of ≥4 mm. Only one ulcer was included from each participant. If a patient had multiple eligible ulcers, the largest ulcer was selected. In cases where ulcers were of equal size, the most recently developed ulcer was included. General exclusion criteria include dementia or any other condition that impaired the ability to give informed consent, as well as the presence of malignant disease. The exact participant numbers and data points used are specified in the respective figure legends. Patient number was determined on the basis of experimental feasibility at the hospital. In vitro and murine data were not blinded, and power analysis was performed and sample sizes are stated in the figure captions.

Materials and reagents

Iron(III) chloride ($FeCl_3$), potassium hexacyanoferrate(III) [$K_3Fe(CN)_6$], potassium chloride (KCl), silica nanoparticles, and aniline were obtained from Sigma-Aldrich. Hydrochloric acid, acetic acid, toluene, ethanol, acetone, and Dulbecco's phosphate-buffered saline (DPBS) were obtained from Thermo Fisher Scientific. Carbon ink (5 wt %) was purchased from NovaCentrix. Gold ink (10 wt %) was purchased from C-INK Co. Ltd. PDMS (SYLGARD 184) was purchased from Dow Corning. Antimicrobial peptide TCP-25 (GKYGFYTHVFRLKKWIQKVIDQFGE) (98% purity, acetate salt) was acquired from CPC Scientific. PET films (50 μm in thickness) were purchased from McMaster-Carr. Before sensor fabrication, 10 μl of 10 wt % poly(styrene-*co*-butadiene) (Sigma-Aldrich) was used to insulate the interconnects and dried overnight.

Fabrication of the sensor patch

Briefly, 50-μm monolayer PET and 100-μm medical tape were precisely cut using a 50-W CO_2 laser cutter (Universal Laser System). The substrates were then cleaned on one side by O_2 plasma surface treatment (Plasma Etch PE-25, 100 W, 10 cm^3 min^{-1} O_2, 150 mtorr) to enhance surface hydrophilicity. Subsequently, gold and carbon electrodes were patterned onto these substrates using an inkjet printer (DMP-2850, Fujifilm). During printing, the plate temperature was maintained at 60°C, followed by overnight heating at 100°C to facilitate rapid evaporation of isopropyl alcohol solvent. Before sensor modification, 10 μl of 10 wt % poly(styrene-*co*-butadiene) (Sigma-Aldrich) was used to insulate the sensor array and dried overnight.

The NO sensors were constructed by engraving 50-μm polyimide sheets and transferring them to PET. GO was synthesized following Hummer's method (*52*). Typically, GO was dispersed in 1.0 ml of CTAB solution (10 mg ml^{-1}) and sonicated for 1 hour to ensure uniform dispersion. Then, Hb (20 mg ml^{-1}) was added to the solution, which was then stored at 4°C overnight to allow for binding. Last, the resultant mixture was drop-cast five times onto the LEG, using 5 μl per application. For the H_2O_2 sensor, PB was deposited onto the Au electrodes through 10 cycles of cyclic voltammetry (CV), ranging from −0.2 to 0.6 V versus Ag/AgCl at a scan rate of 50 mV s^{-1}. This process was conducted in a freshly prepared solution containing 2.5 mM $FeCl_3$, 2.5 mM $K_3[Fe(CN)_6]$, 100 mM KCl, and 100 mM HCl. A thin layer of NiHCF was then deposited using a similar method with a solution of 2.5 mM $NiCl_2$, 2.5 mM $K_3[Fe(CN)_6]$, 100 mM KCl, and 100 mM HCl by two cycles of CV scan from −0.2 to 0.4 V at a scan rate of 50 mV s^{-1}. The NO, O_2, and H_2O_2 working electrodes were protected with 1 μl of 0.2% Nafion solution, respectively.

The pH sensor was prepared by initially cleaning the Au electrode electrochemically in 1 M HCl using CV, sweeping from −0.2

to 1.2 V at a scan rate of 0.1 V s^{-1} for 10 cycles. This was followed by the electrodeposition of a polyaniline pH-sensing film using similar voltammetry conditions for another 10 cycles.

The shared Ag/AgCl reference electrode was constructed by electrodepositing Ag onto the inkjet-printed Au electrode in a solution of 250 mM silver nitrate, 750 mM sodium thiosulfate, and 500 mM sodium bisulfite, using multicurrent steps (20 s each at −1, −5, −10, and −50 μA and −0.1 mA and 100 s at −0.2 mA). Then, the electrode was drop-cast with a 10-μl aliquot of 0.1 M $FeCl_3$ for 1 min to form the Ag/AgCl reference electrode. Next, 1 μl of the reference cocktail membrane (78.1 mg of PVB and 50 mg of NaCl in 1 ml of methanol) was drop-cast on the Ag/AgCl electrode surface and air-dried overnight.

Characterization of biosensors

The cross-sectional architecture of the biosensors was analyzed using focused ion beam–scanning electron microscopy (SEM) (FEI Nova 600 NanoLab). Sensors were directly printed on silicon wafers and cross-sectioned using a glass cutter. Electrochemical characterizations in vitro were performed using a CHI760e electrochemical workstation. All in vitro tests were conducted in SWF, prepared by dissolving 584.4 mg of NaCl, 336.0 mg of $NaHCO_3$, 29.8 mg of KCl, 27.8 mg of $CaCl_2$, and 3.30 g of bovine serum albumin in 100 ml of deionized water, adjusted to a pH of 7.5 unless otherwise specified. The SWF recipe was chosen on the basis of previous reports to mimic the slight alkaline and protein-abundant wound environment (*12*, *53*). NO standard solutions were prepared by gradually adding 2 M H_2SO_4 at a speed of 1 ml $hour^{-1}$ into $NaNO_2$-saturated solution. This was followed by washing with 2 M NaOH solution and then collecting the solution with PBS. All solutions were deoxygenated by purging with N_2 for 10 min before collection. The final concentration of the NO solution was 1.8 mM at room temperature (*31*, *54*).

The NO sensors were characterized using DPV in 0 to 180 μM NO by scanning from −0.5 to −1.0 V with a scan rate of 0.05 mV s^{-1}. O_2 sensors were characterized using DPV scans from 0.2 to −0.6 V with a scan rate of 0.1 mV s^{-1}, with SWF bubbled with N_2 and O_2 to achieve a dissolved O_2 concentration ranging from 0.8 to 7 ppm. The H_2O_2 sensors were characterized chronoamperometrically in 0 to 80 μM H_2O_2 at a potential of 0 V. The pH sensor calibration was performed in McIlvaine buffer using open circuit potential, and the temperature sensor was calibrated by measuring the sensor's resistance.

Fabrication of the microfluidic modules

Janus membranes and wedge channels were prepared by patterning on 50-μm-thick PET and 140-μm-thick medical tape (Adhesives Research) using a 50-W CO_2 laser cutter (Universal Laser System). After inkjet printing and sensor modifications, a silica solution was coated onto the PET surface and medical tape channel by dipping the material in bulk solution for 0.5 s. After complete drying, the hydrophilic area was fabricated by etching with O_2 plasma using a Plasma Etch PE-25 (10 to 20 cm^3 min^{-1} O_2, 100 W, 150 to 200 mtorr) for 15 min. The PET and medical tape layers were then assembled.

For the micropillar structures, a mold was designed in Fusion 360 and fabricated using an ELEGOO Mars 3 3D printer. The micropillars were designed with a diameter of 100 μm and a spacing of 100 μm, with heights ranging from 200 to 800 μm. This mold was then cross-linked under ultraviolet (UV) light exposure overnight and subsequently subjected to heat treatment at 100°C for 24 hours. The molding process was completed by casting PDMS into the mold twice, each time followed by curing at 80°C. The micropillar was then dipped in the silica solution for 5 s. Before assembling the system, the micropillars were etched with O_2 plasma using a Plasma Etch PE-25 (10 to 20 cm^3 min^{-1} O_2, 100 W, 150 to 200 mtorr) for 15 min.

Fabrication of the electronic system

The electronic system was composed of three primary components including power management, data processing with wireless communication, and electrochemical instrumentation. The power management unit used a rechargeable lithium battery (LIR640 with wire, Xinislng). The data processing and wireless communication tasks were handled by a compact PSoC Bluetooth low energy (BLE) module (CYBLE-222014, Cypress Semiconductor), which includes an integrated microcontroller (MCU) and BLE radio. Electrochemical measurements were facilitated by an electrochemical front end (AD5941, Analog Devices), supplemented with voltage buffers (LPV521, Texas Instruments) that support various configurable blocks necessary for electrochemical detection. The whole wireless system required ~300 μW per cycle. For a battery capacity of 9 mA·hour with an output of 3.6 V, it could support 108 cycles of sensor output.

Simulation

Simulation of the wound fluid transport process was conducted through FEA using the commercial software COMSOL Multiphysics. Tetrahedral elements with uniform mesh size allowed modeling of the liquid transport in 3D space. The fluid behavior is described by a Navier-Stokes equation for incompressible flow

$$\rho\left(\frac{\partial v}{\partial t}+(\mathbf{v}\cdot\nabla)\mathbf{v}\right)=-\nabla p+\mu\nabla^2 v$$

$$\nabla\cdot\mathbf{v}=0$$

and phase field equation

$$\frac{\partial\phi}{\partial t}+\mathbf{v}\cdot\nabla\phi=\nabla\frac{\gamma\lambda}{\varepsilon^2}\nabla\Psi$$

$$\Psi=-\nabla\cdot\varepsilon^2\nabla\phi+\left(\phi^2-1\right)\phi$$

$$\lambda=\frac{3\varepsilon\sigma}{2\sqrt{2}}$$

$$\gamma=\chi\varepsilon^2$$

where ϕ, ε, σ, and χ are the phase field parameter, surface thickness control parameter, surface tension coefficient, and mobility tuning parameter, respectively. Here, $\phi = 1$ and -1 represent two flows: liquid and air; ε was set to be the size of the tetrahedral elements; σ was derived for standard material databases for water and air; χ as the mobility tuning parameter was set as 1.

For the Janus membrane model with two-phase flow interface and solid interface, the equation describing the contact angle relationship were

$$n\frac{\gamma\lambda}{\varepsilon^2}\nabla\Psi = 0$$

$$n\,\varepsilon^2\nabla\Psi = \varepsilon^2\cos\theta\,|\nabla\Psi|$$

where θ represents the contact angle of the solid surface.

Cell compatibility

HDF cells (Lonza) were cultured under 37°C and 5% CO_2. Cells were cultured in Dulbecco's modified Eagle's medium (Thermo Fisher Scientific) supplemented with 10% fetal bovine serum (Thermo Fisher Scientific) and 1% penicillin-streptomycin (Thermo Fisher Scientific). Cells were passaged at 70% confluency, and a passage number of 3 to 5 was used for all studies. These cells were cultured directly on the top of sterilized iCares patches. Control group was cultured without iCare patches. Cell viability and metabolic activity were assessed after 3 and 7 days using a live/dead kit (calcein AM/ethidium homodimer-1, Invitrogen) and PrestoBlue assays (Thermo Fisher Scientific), respectively. For the live/dead assay, live cells stained green with calcein AM and dead cells stained red with ethidium homodimer-1 were imaged using an Axio Observer inverted microscope (ZEISS).

Murine diabetic wound model

In vivo testing was conducted using a diabetic wound model in 10-week male db/db (BKS.Cg-Dock7^{m} +/+ Lepr^{db}/J) mice provided by the Jackson Laboratory. This model was confirmed to be diabetic by previously published methods before surgery (*12*). After anesthesia and analgesia, 8-mm full-thickness wounds were created on the dorsomedial skin using a surgical blade, and iCares systems were immediately applied on the wound surface. The wound exudate rate was measured by covering the wound with an occlusive dressing for 24 hours and quantifying the collected volume using a syringe. Silicone adhesive gel (AS1500, CHT) was used to ensure conformal contact, offering a tear resistance of 6.1 N mm^{-1} as specified by the manufacturer. Methicillin-resistant *Staphylococcus aureus* [American Type Culture Collection (ATCC) BAA-2313] and MDR *Escherichia coli* (ATCC BAA-2452) were used for antimicrobial tests. A mixture of a 50-μl solution with 10^8 colony-forming units (CFU) ml^{-1} of each bacterial species was applied on the wound. For treatment, 50 μl of TCP-25 solution was applied three times consecutively to the wound. The control group was treated with 50 μl of 0.9% saline. The skin area adjacent to the wound was sterilized using chlorhexidine scrub and solution. Seven mice were involved in the inoculation test in total.

For biocompatibility assessment, the iCares systems were cut into small pieces and implanted into dorsal subcutaneous skin pockets created with a surgical blade in mice. Tissue samples were then collected on day 14 and day 28 postimplantation. The collected samples were fixed in 4% paraformaldehyde at 4°C overnight and then thoroughly rinsed three times with DPBS. Paraffin embedding sectioning followed, with sections stained with H&E, and immunohistochemistry staining using primary antibodies anti-CD3 [SP7] (ab16669) and secondary antibody goat anti-rabbit IgG H&L (Alexa Fluor 488), along with anti-CD68 [FA-11] antibodies conjugated with PE-cyanine7 (Invitrogen). Sections were counterstained with 4′,6-diamidino-2-phenylindole (DAPI) for visualization of cell nuclei and mounted with ProLong Diamond Antifade Mountant (Invitrogen), and images were captured using an LSM 800 confocal laser scanning microscope (ZEISS).

Evaluation on human patients with chronic wounds

The performance of the iCares was assessed on human patients with chronic wounds. Patients in the Casa Colina Wound Clinic who had chronic lower extremity ulcers due to venous insufficiency or diabetes in the wound clinic were prescreened and subsequently recruited if they agreed to participate. All participants provided written, informed consent before their involvement in the study and use of the pictures. Men or women with active wounds and substantial wound exudate were recruited for the study.

The entire iCares patch was sterilized using UV light for 30 min and subsequently cleaned with alcohol swabs before application to wounds. Data collection commenced once the first drop of wound fluid reached the sensor reservoir and continued for 2 hours. The sensor system persistently captured and transmitted data from the iCares systems. After calibration with standard SWF solutions and simultaneously collected pH and temperature information, the collected data were transformed into concentration concentrations. Calibration was performed after completing each individual test. Kent Imaging technology was used to measure wound oxygen concentrations, serving as the standard benchmark for validating the accuracy of our wearable oxygen sensor.

Machine learning pipeline data preprocessing and feature standardization

Although all the multimodal sensor signals were monitored in real time, data preprocessing and feature extraction was performed asynchronously. The mean value of each person's analyte concentrations was used as the feature to reduce noise in the data and focus on trends rather than outliers. By using the mean value, we were also focusing on reproducible deviations within an individual by smoothing out transient effects. All features were then standardized before entering the machine learning pipeline by adjusting the features to have a mean of zero and an SD of 1. After data collection and analysis, we randomly shuffled and divided the datasets for training and testing in an 80:20 ratio, using stratified sampling to preserve class balance among different wound healing trajectories. To further ensure generalizability and mitigate the risk of overfitting, the models underwent cross-validation, with data evenly distributed across each fold. Data points were then randomly chosen, ensuring balanced representation from each class. We further asserted the reproducibility of the results by iterating 250 times across different splitting patterns to ensure that the results were not biased toward any dataset. Test error was then compiled across all iterations, where the reported accuracy is the mean of this distribution. This ensures that others can train a similar model and get an accuracy within an expected deviation from our initial results.

Machine learning model selection, building, and training

All training models were built using Python (v.3.8) based on the data collected from 20 patients with chronic wounds. The ML model was developed to link biological and chemical features to wound classification, healing time, and depth from clinician estimations. Models were built by leveraging libraries such as Scikit-learn for

implementing machine learning algorithms. Several machine learning models were evaluated according by their precision-recall curves and F_1 scores, including linear, radial basis function, and sigmoid function of SVCs, as well as *k*-nearest neighbor algorithm (KNN). The SVC models were used to explore the separability of data in high-dimensional spaces using various kernel functions. For each algorithm, we tuned the hyperparameters through grid search, adjusting factors such as the penalty parameter in SVC and the number of neighbors in KNN. This allowed us to evaluate the best performing model architecture for each patient's wound classification and prognosis prediction. The SVC linear model was found to be optimal for wound classification, healing time prediction, and wound depth estimation.

Statistical analysis

Statistical analyses were performed using the commercial software packages GraphPad Prism and Origin (Pro) (version 2022, OriginLab Corporation). All measurements were conducted with at least three replicates unless otherwise stated in the figure captions. Data were assumed to be normally distributed but were not statistically tested for normality. Data are presented as means ± SD. Statistical significance was assessed using unpaired two-tailed Student's *t* test between two groups and one-way analysis of variance (ANOVA) for analyzing three or more groups, with $P < 0.05$ considered statistically significant. All tabular data are available in data file S1.

Supplementary Materials

The PDF file includes:

Figs. S1 to S44
Tables S1 to S4
Legend for data file S1
Legends for movies S1 to S7
References (*55*, *56*)

Other Supplementary Material for this manuscript includes the following:

Data file S1
Movies S1 to S7
MDAR Reproducibility Checklist

REFERENCES AND NOTES

1. V. Falanga, R. R. Isseroff, A. M. Soulika, M. Romanelli, D. Margolis, S. Kapp, M. Granick, K. Harding, Chronic wounds. *Nat. Rev. Dis. Primers* **8**, 50 (2022).
2. D. G. Armstrong, A. J. M. Boulton, S. A. Bus, Diabetic foot ulcers and their recurrence. *N. Engl. J. Med.* **376**, 2367–2375 (2017).
3. D. G. Armstrong, T.-W. Tan, A. J. M. Boulton, S. A. Bus, Diabetic foot ulcers: A review. *JAMA* **330**, 62 (2023).
4. S. O. Oyibo, E. B. Jude, I. Tarawneh, H. C. Nguyen, L. B. Harkless, A. J. M. Boulton, A comparison of two diabetic foot ulcer classification systems. *Diabetes Care* **24**, 84–88 (2001).
5. T. B. Santema, E. A. Lenselink, R. Balm, D. T. Ubbink, Comparing the Meggitt-Wagner and the University of Texas wound classification systems for diabetic foot ulcers: Inter-observer analyses. *Int. Wound J.* **13**, 1137–1141 (2016).
6. A. Bravo-Molina, J. P. Linares-Palomino, B. Vera-Arroyo, L. M. Salmerón-Febres, E. Ros-Díe, Inter-observer agreement of the Wagner, University of Texas and PEDIS classification systems for the diabetic foot syndrome. *Foot Ankle Surg.* **24**, 60–64 (2018).
7. C. Wang, E. Shirzaei Sani, C.-D. Shih, C. T. Lim, J. Wang, D. G. Armstrong, W. Gao, Wound management materials and technologies from bench to bedside and beyond. *Nat. Rev. Mater.* **9**, 550–566 (2024).
8. Y. Gao, D. T. Nguyen, T. Yeo, S. B. Lim, W. X. Tan, L. E. Madden, L. Jin, J. Y. K. Long, F. A. B. Aloweni, Y. J. A. Liew, M. L. L. Tan, S. Y. Ang, S. D. O. Maniya, I. Abdelwahab, K. P. Loh, C.-H. Chen, D. L. Becker, D. Leavesley, J. S. Ho, C. T. Lim, A flexible multiplexed immunosensor for point-of-care in situ wound monitoring. *Sci. Adv.* **7**, eabg9614 (2021).
9. Z. Ge, W. Guo, Y. Tao, H. Sun, X. Meng, L. Cao, S. Zhang, W. Liu, M. L. Akhtar, Y. Li, Y. Ren, Wireless and closed-loop smart dressing for exudate management and on-demand treatment of chronic wounds. *Adv. Mater.* **35**, 2304005 (2023).
10. Y. Jiang, A. A. Trotsyuk, S. Niu, D. Henn, K. Chen, C.-C. Shih, M. R. Larson, A. M. Mermin-Bunnell, S. Mittal, J.-C. Lai, A. Saberi, E. Beard, S. Jing, D. Zhong, S. R. Steele, K. Sun, T. Jain, E. Zhao, C. R. Neimeth, W. G. Viana, J. Tang, D. Sivaraj, J. Padmanabhan, M. Rodrigues, D. P. Perrault, A. Chattopadhyay, Z. N. Maan, M. C. Leeolou, C. A. Bonham, S. H. Kwon, H. C. Kussie, K. S. Fischer, G. Gurusankar, K. Liang, K. Zhang, R. Nag, M. P. Snyder, M. Januszyk, G. C. Gurtner, Z. Bao, Wireless, closed-loop, smart bandage with integrated sensors and stimulators for advanced wound care and accelerated healing. *Nat. Biotechnol.* **41**, 652–662 (2023).
11. C. Wang, E. Shirzaei Sani, W. Gao, Wearable bioelectronics for chronic wound management. *Adv. Funct. Mater.* **32**, 2111022 (2022).
12. E. Shirzaei Sani, C. Xu, C. Wang, Y. Song, J. Min, J. Tu, S. A. Solomon, J. Li, J. L. Banks, D. G. Armstrong, W. Gao, A stretchable wireless wearable bioelectronic system for multiplexed monitoring and combination treatment of infected chronic wounds. *Sci. Adv.* **9**, eadf7388 (2023).
13. J. Tu, J. Min, Y. Song, C. Xu, J. Li, J. Moore, J. Hanson, E. Hu, T. Parimon, T.-Y. Wang, E. Davoodi, T.-F. Chou, P. Chen, J. J. Hsu, H. B. Rossiter, W. Gao, A wireless patch for the monitoring of C-reactive protein in sweat. *Nat. Biomed. Eng.* **7**, 1293–1306 (2023).
14. J. Shi, S. Kim, P. Li, F. Dong, C. Yang, B. Nam, C. Han, E. Eig, L. L. Shi, S. Niu, J. Yue, B. Tian, Active biointegrated living electronics for managing inflammation. *Science* **384**, 1023–1030 (2024).
15. J. W. Song, H. Ryu, W. Bai, Z. Xie, A. Vázquez-Guardado, K. Nandoliya, R. Avila, G. Lee, Z. Song, J. Kim, M.-K. Lee, Y. Liu, M. Kim, H. Wang, Y. Wu, H.-J. Yoon, S. S. Kwak, J. Shin, K. Kwon, W. Lu, X. Chen, Y. Huang, G. A. Ameer, J. A. Rogers, Bioresorbable, wireless, and battery-free system for electrotherapy and impedance sensing at wound sites. *Sci. Adv.* **9**, eade4687 (2023).
16. X. Xiao, X. Xiao, A. Nashalian, A. Libanori, Y. Fang, X. Li, J. Chen, Triboelectric nanogenerators for self-powered wound healing. *Adv. Healthc. Mater.* **10**, e2100975 (2021).
17. N. T. Garland, J. W. Song, T. Ma, Y. J. Kim, A. Vázquez-Guardado, A. B. Hashkavayi, S. K. Ganeshan, N. Sharma, H. Ryu, M. Lee, B. Sumpio, M. A. Jakus, V. Forsberg, R. Kaveti, S. K. Sia, A. Veves, J. A. Rogers, G. A. Ameer, A. J. Bandodkar, A miniaturized, battery-free, wireless wound monitor that predicts wound closure rate early. *Adv. Healthc. Mater.* **12**, 2301280 (2023).
18. G. Schultz, G. Tariq, K. Harding, K. Carville, M. Romanelli, P. Chadwick, S. Percival, Z. Moore, *WUWHS Consensus Document—Wound Exudate: Effective Assessment and Management* (Wounds International, 2019).
19. C. Dealey, J. Cameron, M. Arrowsmith, A study comparing two objective methods of quantifying the production of wound exudate. *J. Wound Care* **15**, 149–153 (2006).
20. L. Shi, X. Liu, W. Wang, L. Jiang, S. Wang, A self-pumping dressing for draining excessive biofluid around wounds. *Adv. Mater.* **31**, 1804187 (2019).
21. X. Jiang, P. B. Lillehoj, Microneedle-based skin patch for blood-free rapid diagnostic testing. *Microsyst. Nanoeng.* **6**, 96 (2020).
22. C. Dunnill, T. Patton, J. Brennan, J. Barrett, M. Dryden, J. Cooke, D. Leaper, N. T. Georgopoulos, Reactive oxygen species (ROS) and wound healing: The functional role of ROS and emerging ROS-modulating technologies for augmentation of the healing process. *Int. Wound J.* **14**, 89–96 (2017).
23. A. E. K. Loo, Y. T. Wong, R. Ho, M. Wasser, T. Du, W. T. Ng, B. Halliwell, Effects of hydrogen peroxide on wound healing in mice in relation to oxidative damage. *PLOS ONE* **7**, e49215 (2012).
24. J. Luo, A. F. Chen, Nitric oxide: A newly discovered function on wound healing. *Acta Pharmacol. Sin.* **26**, 259–264 (2005).
25. A. Schwentker, T. R. Billiar, Nitric oxide and wound repair. *Surg. Clin. N. Am.* **83**, 521–530 (2003).
26. A. A. Tandara, T. A. Mustoe, Oxygen in wound healing—More than a nutrient. *World J. Surg.* **28**, 294–300 (2004).
27. H. W. Hopf, M. D. Rollins, Wounds: An overview of the role of oxygen. *Antioxid. Redox Signal.* **9**, 1183–1192 (2007).
28. S. Schreml, R. M. Szeimies, L. Prantl, S. Karrer, M. Landthaler, P. Babilas, Oxygen in acute and chronic wound healing: Oxygen in wound healing. *Br. J. Dermatol.* **163**, 257–268 (2010).
29. R. Li, H. Qi, Y. Ma, Y. Deng, S. Liu, Y. Jie, J. Jing, J. He, X. Zhang, L. Wheatley, C. Huang, X. Sheng, M. Zhang, L. Yin, A flexible and physically transient electrochemical sensor for real-time wireless nitric oxide monitoring. *Nat. Commun.* **11**, 3207 (2020).
30. Y. Ha, J. Sim, Y. Lee, M. Suh, Insertable fast-response amperometric NO/CO dual microsensor: Study of neurovascular coupling during acutely induced seizures of rat brain cortex. *Anal. Chem.* **88**, 2563–2569 (2016).
31. W. Wen, W. Chen, Q.-Q. Ren, X.-Y. Hu, H.-Y. Xiong, X.-H. Zhang, S.-F. Wang, Y.-D. Zhao, A highly sensitive nitric oxide biosensor based on hemoglobin–chitosan/graphene–hexadecyltrimethylammonium bromide nanomatrix. *Sens. Actuators B* **166–167**, 444–450 (2012).

32. C. Xu, Y. Song, J. R. Sempionatto, S. A. Solomon, Y. Yu, H. Y. Y. Nyein, R. Y. Tay, J. Li, W. Heng, J. Min, A. Lao, T. K. Hsiai, J. A. Sumner, W. Gao, A physicochemical-sensing electronic skin for stress response monitoring. *Nat. Electron.* **7**, 168–179 (2024).
33. J. E. Grey, S. Enoch, K. G. Harding, Wound assessment. *BMJ* **332**, 285–288 (2006).
34. S. Lundberg, S.-I. Lee, A unified approach to interpreting model predictions. arXiv:1705.07874 [cs.AI] (2017).
35. M. Mittal, M. R. Siddiqui, K. Tran, S. P. Reddy, A. B. Malik, Reactive oxygen species in inflammation and tissue injury. *Antioxid. Redox Signal.* **20**, 1126–1167 (2014).
36. W. Razzell, I. R. Evans, P. Martin, W. Wood, Calcium flashes orchestrate the wound inflammatory response through DUOX activation and hydrogen peroxide release. *Curr. Biol.* **23**, 424–429 (2013).
37. M. J. Malone-Povolny, S. E. Maloney, M. H. Schoenfisch, Nitric oxide therapy for diabetic wound healing. *Adv. Healthc. Mater.* **8**, e1801210 (2019).
38. M. Shi, Z. Du, Y. Qi, W. Li, H. Hu, X. Lin, S. Wang, Z. Tang, M. Zhou, Wound microenvironment-responsive glucose consumption and hydrogen peroxide generation synergistic with azithromycin for diabetic wounds healing. *Theranostics* **12**, 2658–2673 (2022).
39. S. Schreml, R. M. Szeimies, L. Prantl, S. Karrer, M. Landthaler, P. Babilas, Oxygen in acute and chronic wound healing. *Br. J. Dermatol.* **163**, 257–268 (2010).
40. S. Roy, S. Khanna, K. Nallu, T. K. Hunt, C. K. Sen, Dermal wound healing is subject to redox control. *Mol. Ther.* **13**, 211–220 (2006).
41. M. Carlström, Nitric oxide signalling in kidney regulation and cardiometabolic health. *Nat. Rev. Nephrol.* **17**, 575–590 (2021).
42. G. Ren, P. T. J. Hwang, R. Millican, J. Shin, B. C. Brott, T. van Groen, C. M. Powell, S. Bhatnagar, M. E. Young, H. W. Jun, J. A. Kim, Subcutaneous administration of a nitric oxide-releasing nanomatrix gel ameliorates obesity and insulin resistance in high-fat diet-induced obese mice. *ACS Appl. Mater. Interfaces* **14**, 19104–19115 (2022).
43. Z. Bahadoran, P. Mirmiran, A. Ghasemi, Role of nitric oxide in insulin secretion and glucose metabolism. *Trends Endocrinol. Metab.* **31**, 118–130 (2020).
44. P. J. Meakin, B. M. Coull, Z. Tuharska, C. McCaffery, I. Akoumianakis, C. Antoniades, J. Brown, K. J. Griffin, F. Platt, C. H. Ozber, N. Y. Yuldasheva, N. Makava, A. Skromna, A. Prescott, A. D. McNeilly, M. Siddiqui, C. N. Palmer, F. Khan, M. L. Ashford, Elevated circulating amyloid concentrations in obesity and diabetes promote vascular dysfunction. *J. Clin. Invest.* **130**, 4104–4117 (2020).
45. N. W. Rajapakse, G. A. Head, D. M. Kaye, Say NO to obesity-related hypertension: Role of the L-arginine-nitric oxide pathway. *Hypertension* **67**, 813–819 (2016).
46. M. Ottolini, K. Hong, E. L. Cope, Z. Daneva, L. J. DeLalio, J. D. Sokolowski, C. Marziano, N. Y. Nguyen, J. Altschmied, J. Haendeler, S. R. Johnstone, M. Y. Kalani, M. S. Park, R. P. Patel, W. Liedtke, B. E. Isakson, S. K. Sonkusare, Local peroxynitrite impairs endothelial transient receptor potential vanilloid 4 channels and elevates blood pressure in obesity. *Circulation* **141**, 1318–1333 (2020).
47. Y. Iwakiri, M. Y. Kim, Nitric oxide in liver diseases. *Trends Pharmacol. Sci.* **36**, 524–536 (2015).
48. M. D. Brown, M. H. Schoenfisch, Electrochemical nitric oxide sensors: Principles of design and characterization. *Chem. Rev.* **119**, 11551–11575 (2019).
49. M. Berezo, J. Budman, D. Deutscher, C. T. Hess, K. Smith, D. Hayes, Predicting chronic wound healing time using machine learning. *Adv. Wound Care* **11**, 281–296 (2022).
50. M. C. Robson, D. P. Hill, M. E. Woodske, D. L. Steed, Wound healing trajectories as predictors of effectiveness of therapeutic agents. *Arch. Surg.* **135**, 773–777 (2000).
51. S. K. Cho, S. Mattke, H. Gordon, M. Sheridan, W. Ennis, Development of a model to predict healing of chronic wounds within 12 weeks. *Adv. Wound Care* **9**, 516–524 (2020).
52. W. S. Hummers, R. E. Offeman, Preparation of graphitic oxide. *J. Am. Chem. Soc.* **80**, 1339–1339 (1958).
53. A. U. Svensby, E. Nygren, A. Gefen, B. Cullen, Å. M. Ronkvist, A. Gergely, M. D. Craig, The importance of the simulated wound fluid composition and properties in the determination of the fluid handling performance of wound dressings. *Int. Wound J.* **21**, e14861 (2024).
54. A. R. Butler, D. L. H. Williams, The physiological role of nitric oxide. *Chem. Soc. Rev.* **22**, 233–241 (1993).
55. S. Cho, J.-H. Ha, J. Ahn, H. Han, Y. Jeong, S. Jeon, S. Hwang, J. Choi, Y. S. Oh, D. Kim, S. A. Park, D. Lee, J. Ahn, B. Kang, B.-H. Kang, J.-H. Jeong, I. Park, Wireless, battery-free, optoelectronic diagnostic sensor integrated colorimetric dressing for advanced wound care. *Adv. Funct. Mater.* **34**, 2316196 (2024).
56. N. T. Garland, J. W. Song, T. Ma, Y. J. Kim, A. Vázquez-Guardado, A. B. Hashkavayi, S. K. Ganeshan, N. Sharma, H. Ryu, M.-K. Lee, B. Sumpio, M. A. Jakus, V. Forsberg, R. Kaveti, S. K. Sia, A. Veves, J. A. Rogers, G. A. Ameer, A. J. Bandodkar, A. Miniaturized, Battery-free, wireless wound monitor that predicts wound closure rate early. *Adv. Healthc. Mater.* **12**, 2301280 (2023).

Acknowledgments: We gratefully acknowledge the critical support and infrastructure provided for this work by the Kavli Nanoscience Institute at Caltech. J.M. acknowledges fellowship support from the National Institutes of Health Training grant (T32EB023858). We also acknowledge the support from the Research Institute in the Casa Colina Hospital and Centers for Healthcare in Pomona, CA. We thank the participants who contributed their time for the study. We acknowledge the support from E. R. Rosario, Director of the Research Institute at Casa Colina Hospital and Centers for Healthcare, and E. Ortega for coordinating the study. **Funding:** This study was funded by the National Institutes of Health grants R01HL155815 (to W.G.), R21DK13266 (to W.G.), and R01DK124789 (to D.G.A.); National Science Foundation grants 2145802 (to W.G.) and 2052578 (to D.G.A.); American Cancer Society grant RSG-21-181-01-CTPS (to W.G.); Army Research Office grant W911NF-23-1-0041 (to W.G.); US Army Medical Research Acquisition Activity grant HT9425-24-1-0249 (to W.G.); and Heritage Medical Research Institute (to W.G.). **Author contributions:** C.W. and W.G. conceived the project. C.W., K.F., and W.G. developed the methodology. C.W., K.F., E.S.S., J.A.L.-R., S.S., M.W., and A.S. developed and characterized the iCare systems. C.W. performed characterization and tests on cells, bacteria, and animals. C.W., K.F., and C.-D.S. performed patient studies. C.W., W.H., and J.M. developed the PCB and evaluation. J.L. performed simulations. K.F., H.H., and G.K. assisted in the SEM imaging. C.W. and S.A.S. performed machine learning analysis of patient data. W.G. and D.G.A. acquired funding. W.G., C.-D.S., and D.G.A. supervised the whole project. C.W., K.F., and W.G. wrote the original draft. C.W., K.F., E.S.S., J.A.L.-R., W.H., J.M., S.A.M., M.W., J.L., H.H., G.K., S.S., A.S., C.-D.S., D.G.A., and W.G. edited the manuscript for review. **Competing interests:** W.G. is a cofounder and advisor at Persperity Health. All other authors declare that they have no competing interests. **Data and materials availability:** All data associated with this study are present in the paper or the Supplementary Materials. All codes related to the analysis presented are available at https://doi.org/10.5281/zenodo.14773650.

Submitted 11 September 2024
Resubmitted 4 December 2024
Accepted 3 April 2025
Published 23 April 2025
10.1126/scitranslmed.adt0882